Microstructure design and mechanical properties in a near-α Ti–4Mo alloy

Z. Tarzimoghadam, S. Sandlöbes *, K.G. Pradeep, D. Raabe

Max-Planck-Institut für Eisenforschung GmbH, Max-Planck-Straße 1, 40237 Düsseldorf, Germany

ARTICLE INFO

ABSTRACT

We study the effects of different heat treatment routes on microstructure engineering and the resulting mechanical response in a plain binary Ti–4Mo (wt%) model alloy. We observe a broad variety of microstructure formation mechanisms including diffusion driven allotropic phase transformations as well as shear and/or diffusion dominated modes of martensitic transformations, enabling a wealth of effective microstructure design options even in such a simple binary Ti alloy. This wide variety of microstructures allows tailoring the mechanical properties ranging from low yield strength (350 MPa) and high ductility (30–35% tensile elongation) to very high yield strength (1100 MPa) and medium ductility (10–15% tensile elongation) as well as a variety of intermediate states.

Mechanical testing and microstructure characterization using optical microscopy, scanning electron microscopy based techniques, transmission electron microscopy and atom probe tomography were performed revealing that minor variations in the heat treatment cause significant changes in the resulting microstructures (e.g. structural refinement, transition between diffusive and martensitic transformations). The experimental results on microstructure evolution during the applied different heat treatment routes are discussed with respect to the mechanical properties.

© 2015 Acta Materialia Inc. Published by Elsevier Ltd. All rights reserved.

1. Introduction

Titanium and its alloys exhibit an excellent combination of mechanical and physical properties for key applications in aerospace, energy and chemical industry [1–3]. The mechanical properties of titanium alloys are important criteria for the material service capabilities both in aerospace and industrial applications. Most titanium alloys used in structural applications consist of two-phase mixtures of α and β phases combined in different morphologies and relative volume fractions [4,8]. Two-phase α + β alloys offer a range of combinations of strength, toughness and high temperature properties up to ∼600 °C [4–6]. Solid state phase transformations are the main factors determining the functional characteristics of these alloys. Manipulation of the mechanical properties depends on the effect of alloying additions and thermo-mechanical processing on the stability and mechanical behavior of the two phases, both individually and in a variety of microstructural combinations [4,7,9].

The solid-state β → β + α transformation in titanium alloys can take place either diffusionless, i.e. martensitic, or by diffusion controlled nucleation and growth processes depending on cooling rate and alloy composition. This transition in transformation kinetics and kinematics enables the design of complex microstructures with features spanning across a broad range of length scales [10]. Thermo-mechanical processing is a useful method to tailor the microstructure and, thus, to control the size and morphology of different phases in Ti alloys [11–14]. Particularly, the control of the morphology of the α phase is one of the most important keys to improve the properties of α + β Ti alloys [4,12,15–17]. The mechanical properties of two-phase (α + β) titanium alloys are very sensitive to the morphology and geometrical arrangement of the two phases, similar as in dual phase steels [18,19]. A fully lamellar structure is characterized by high fatigue crack propagation resistance and high fracture toughness. Important parameters for a lamellar microstructure with respect to the mechanical properties are the β-grain size, the size of the colonies of α-phase lamellae, the thickness of the α-lamellae, and the nature of the inter-lamellar interfaces (β-phase) [20–22]. One of the most influential microstructural parameters is the α colony size since it determines the effective slip length in lamellar microstructures [21–23]. The cooling rate from the homogenization temperature determines the α colony size and width of the α-lamellae within the β grains and the extent of continuous α-layers at β grain boundaries [7,21,24–26].

* Corresponding author.
  E-mail address: s.sandloebes@mpie.de (S. Sandlöbes).

Most of these earlier studies use more complex ternary or quaternary Ti-alloys and include variations in the alloying content. In this study we systematically investigate microstructure variations by different heat treatment routes in a plain binary Ti–4Mo (wt%) alloy. Specifically, we study segregation, partitioning and phase transformation mechanisms and their impact on microstructural variations in order to tailor the mechanical properties. For the same alloy composition we observe a huge variety of different mechanisms of microstructure formation including diffusion driven allotropic phase transformations as well as shear and/or diffusion dominated modes of martensitic transformations. Such a high variety of solid-state phase transitions and transformations in one simple binary alloy is known only from binary Fe–C alloys [27,28], where minor variations in the heat treatment conditions significantly affect the local C-distribution, the phase transformation reactions, the resulting microstructure and the macroscopic properties. Here we compare the influence of heat treatments at different annealing temperatures and different cooling rates on the occurring phase transformation reactions and the associated microstructural evolution as well as their impact on the resulting mechanical properties in a basic binary Ti–4Mo alloy.

2. Experimental procedure

The Ti–4Mo alloy was produced using an electric arc furnace under Ar atmosphere and cast in a copper mold. Table 1 shows the chemical composition of the as-cast alloy. The as-cast billets were subjected to high-strain-rate unidirectional hot rolling at 875 °C (β phase region) with 50% thickness reduction per pass.

Fig. 1 shows the Ti–Mo binary phase diagram. The alloy composition and heat treatment temperatures are indicated in the diagram.

To investigate the range of mechanical properties with respect to the underlying microstructural changes in this alloy different annealing and cooling treatments were applied, Fig. 2:

(i) Annealing in the β phase region at 950 °C for 30 min and then furnace cooling (Fig. 2a). The cooling rate was: 950–500 °C: 45 K/min, 500 °C – room temperature: 4 K/min.
(ii) Annealing at 550 °C for 6 h in the α + β region (temperature with the highest Mo content in the α phase, i.e. highest Mo concentration and most homogeneous distribution of Mo in the α phase) and then furnace cooling. Subsequent annealing at 800 °C in the two phase α + β region for 30 min and water quenching (Fig. 2b).
(iii) Annealing at 550 °C for 6 h in the α + β region (temperature with the highest Mo content in the α phase, i.e. highest Mo concentration and most homogeneous distribution of Mo in the α phase) and furnace cooling. Subsequent annealing at 950 °C in the β phase region for 30 min and water quenching (Fig. 2c).
(iv) Annealing at 950 °C in the β region with 30 min holding time, followed by water quenching (Fig. 2d).
(v) Annealing at 950 °C in the β region with 30 min holding time followed by water quenching. Subsequent tempering for 1 h at 550 °C and furnace cooling (Fig. 2e). The cooling rate was: 550–250 °C: 15 K/min, 250 °C – room temperature: 4.75 K/min.
(vi) Annealing at 950 °C in the β region with 30 min holding time followed by water quenching. Subsequent cyclic heat treatment (4 cycles) between the α + β and the β region (900 °C and 650 °C, respectively) with 5 min holding time in each region (Fig. 2f).

Table 1
Chemical composition of the as cast alloy.

Sample	Mo [wt%]	C [wt%]	N [wt%]	O [wt%] [a]
LBO 411-12; 4% Mo	3.80	0.022	0.0052	0.140

[a] O < 0.18 wt%, corresponding to Grade 1 CP Ti, (CP: commercial purity standard).
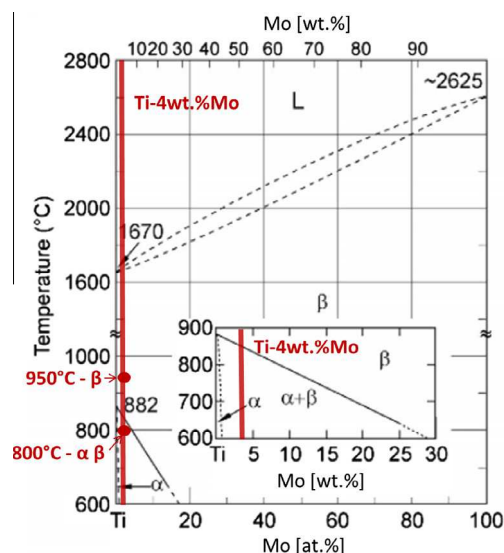

Fig. 1. Ti–Mo binary phase diagram showing also the alloy composition and heat treatment temperatures in red; modified image from [7]. (For interpretation of the references to color in this figure legend, the reader is referred to the web version of this article.)

All heating and furnace cooling processes were performed under Ar atmosphere.

Table 2 lists the heat treatments conducted in this study and the corresponding abbreviations as used throughout the paper.

Tensile tests were conducted at room temperature on specimens with gauge dimensions of 2 mm width × 4 mm length × 1 mm thickness with an initial strain rate of 10^{-3} s^{-1} until fracture. The monotonic tensile deformation experiments were carried out on a tensile test instrument by Kammrath & Weiss GmbH equipped with a digital image correlation (DIC) system (ARAMIS system, GOM) to measure simultaneously stress, strain and the spatial strain distribution. Details of this set-up are described in [29].

For optical microscopy observations the specimens were chemically etched using a mixture of 75 ml Glycerin, 16 ml HNO$_3$ and 16 ml HF. Optical micrographs were acquired using a LEICA DM4000M light optical microscope.

Electron backscatter diffraction (EBSD) orientation mapping was performed in a Zeiss scanning electron microscope (SEM) (XB 1540, Carl Zeiss SMT AG, Germany) equipped with a TSL OIM EBSD system at 15 kV acceleration voltage. Energy dispersive X-ray spectroscopy (EDS) was done using an Apollo XL Silicon Drift Detector in combination with EBSD to analyze the elemental partitioning.

Discs with a diameter of 3 mm and 1 mm height were cut by spark erosion and mechanically ground to a thickness of ~100 μm. Electron-transparent foils were prepared by double-jet electro-polishing using an electrolyte consisting of 65 vol.% methanol, 35 vol.% butanol, and 5 vol.% perchloric acid at a voltage of ~31 V at −30 °C. The thin foils were examined using a Philips CM20 and a Jeol 2200FS transmission electron microscope (TEM) both operated at an acceleration voltage of 200 kV.
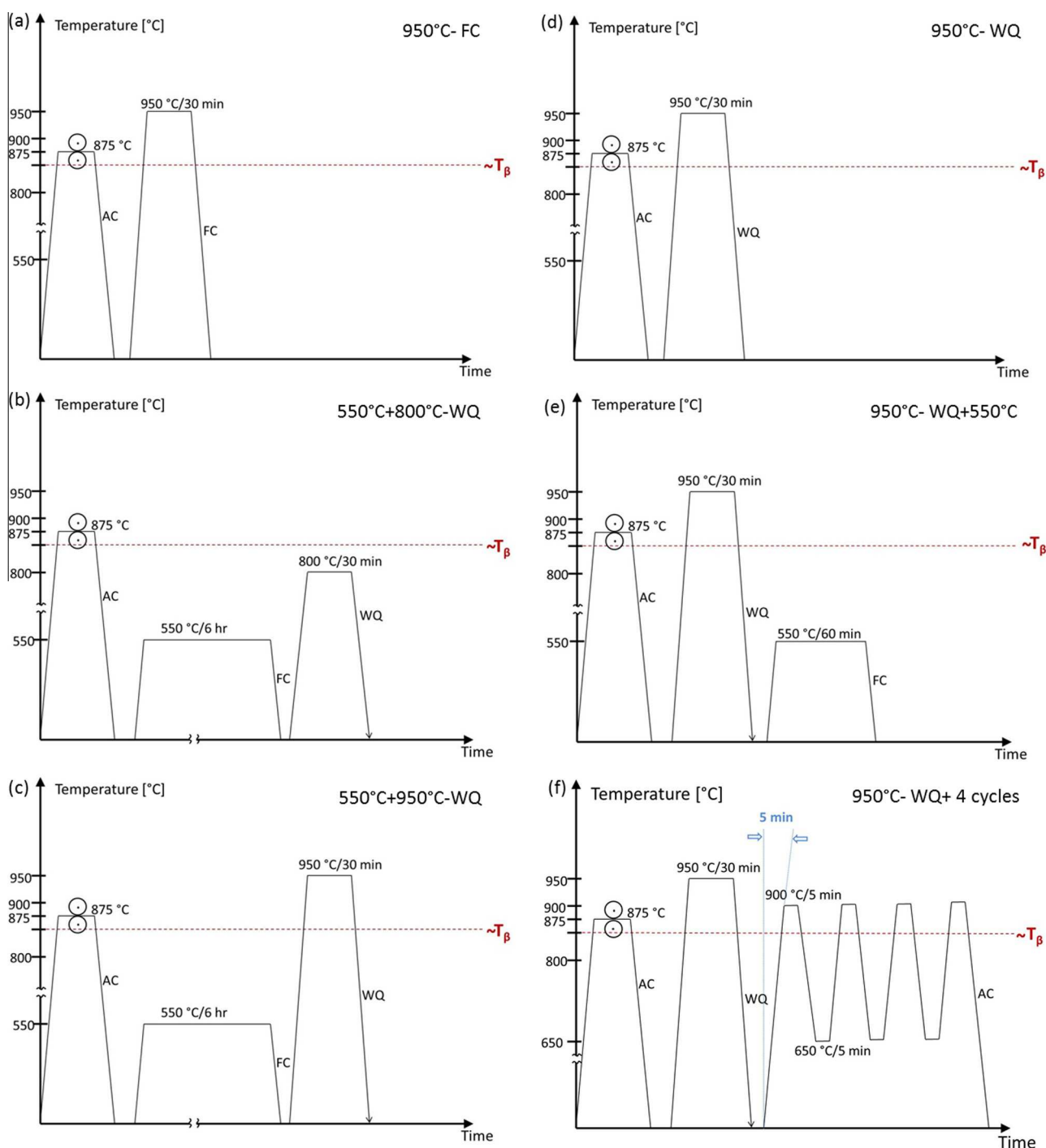
Fig. 2. Schematic drawings of the applied heat treatment routes, (a) 950 °C-FC, (b) 550 °C + 800 °C-WQ, (c) 550 °C + 950 °C-WQ, (d) 950 °C-WQ, (e) 950 °C-WQ + 550 °C, (f) 950 °C-WQ + 4 cycles; AC: air cooling, WQ: water quenching, FC: furnace cooling.

Atomic-scale chemical analysis was conducted using atom probe tomography (APT). APT samples were prepared site specific using focused ion beam (FIB) (dual-beam FEI Helios Nanolab 600) following the procedure described in [30]. Pulsed voltage APT was performed using a local electrode atom probe (LEAP 3000X HR, Cameca Instruments) at a specimen temperature of 60 K. The pulse frequency was kept at 200 kHz. Data analysis was performed using the software IVAS 3.6.6 provided by Cameca Instruments.

3. Results

Fig. 3 shows the engineering stress-strain curves of the Ti–4Mo alloy after different heat treatments. It is evident that the mechanical properties change significantly with the heat treatment conditions. Annealing at 950 °C (β-region) followed by furnace cooling (950 °C-FC) results in a tensile strength of 500 MPa and 25% elongation to fracture. Annealing in the α + β region and subsequent water quenching (550 °C + 800 °C-WQ) gives an increase in tensile

Table 2
Different heat treatment routes and corresponding abbreviations as used throughout.

Heat treatment	Corresponding nomenclature
950 °C, 30 min, furnace cooling[*]	950 °C-FC
550 °C, 6 h, furnace cooling + 800 °C, 30 min, water quenching	550 °C + 800 °C-WQ
550 °C, 6 h, furnace cooling + 950 °C, 30 min, water quenching	550 °C+950 °C-WQ
950 °C, 30 min, water quenching	950 °C-WQ
950 °C, 30 min, water quenching + 550 °C, 60 min, furnace cooling	950 °C-WQ+550 °C
950 °C, 30 min, water quenching + 4 cycles between 900 °C and 650 °C, 5 min holding time each, followed by air cooling	950 °C-WQ + 4 cycles

[*] Cooling rate: 950–500 °C: 45 K/min, 500 °C – room temperature: 4 K/min.

strength of about 100 MPa and a slight decrease (to 22.5%) of the elongation to fracture. Annealing at 950 °C and water quenching (550 °C + 950 °C-WQ) brings a tensile strength of 1100 MPa and 12% elongation to fracture, which is twice the strength and half the elongation than observed for annealing at 950 °C and furnace cooling. Tensile tests after heat treatments 950 °C-WQ, 950 °C-WQ +550 °C and 950 °C-WQ + 4 cycles (Fig. 3b) show that the tensile strength decreases and ductility increases upon tempering the water quenched structure. Cyclic heat treatment at 550 °C similarly results in a further decrease of the tensile strength concomitant with an increase of the tensile elongation to fracture.

Fig. 4 shows light optical micrographs of the microstructures of Ti–4Mo subjected to heat treatments 950 °C-FC, 550 °C + 800 °C-WQ and 550 °C + 950 °C-WQ and Figs. 5–7 present EBSD analyses in terms of image quality (IQ) maps, phase maps and inverse pole figure (IPF) maps of Ti–4Mo after heat treatment routes 950 °C-FC, 550 °C + 800 °C-WQ, 550 °C + 950 °C-WQ, 950 °C-WQ, 950 °C-WQ + 550 °C, 950 °C-WQ + 4 cycles.

All EBSD measurements were performed with a small step size of 50 nm to identify and index the fine α/β lamellar structures. The image quality and phase maps show the different dispersions and morphologies of α and β and the IPF maps present the corresponding orientations of α and β, respectively. From the EBSD results the number of planes between the two phases that match the Burger orientation relationship (BOR) was calculated using a maximum plane misorientation of 2°. The

Burgers orientation relationship between α and β phase crystals $((110)_\beta||(0002)_\alpha;\ [1\bar{1}1]_\beta||[11\bar{2}0]_\alpha)$ was confirmed in all cases, as shown by corresponding stereographic projections for the different heat treatments in Figs. 5–7.

Annealing at 950 °C followed by furnace cooling (950 °C-FC) results in a transformed-β structure consisting of colonies of α/β lamellae and grain boundary α decorating the prior β-grain boundaries (Figs. 4a and 5a). The α-laths pertain to the same crystallographic variant, Fig. 5a-(iii). Annealing in the two phase region below the β-transus temperature (550 °C + 800 °C-WQ) causes softening of the α lamellae at the edges, Fig. 5b-(ii). The resulting microstructure is a dual-phase structure with globular and lamellar α phase grains (Figs. 4b and 5b) including coarse colonies of α with a typical basket-weave structure with a multi-variant distribution of small colonies and retained β phase.

The Ti–4Mo sample water-cooled from the β region (550 °C + 950 °C-WQ) reveals a transformed β structure with a high density of α lamellae colonies within the prior β grains (Figs. 4c and 6a). A continuous network of grain boundary α along the entire prior-β grains as in 950 °C-FC is not present. The alloy transformed to martensite during water-quenching from the β-phase field.

The fine α/β lamellae structure observed for 950 °C-FC and 550 °C + 800 °C-WQ is clearly visible from the image quality and phase maps in Fig. 5a and b. By reducing the annealing temperature to 800 °C, hence shifting it into the α + β region, the volume fraction and lamellae thickness of retained β phase is increased when compared to 950 °C-FC (volume fraction of about 0.5 in 950 °C-FC; volume fraction of about 2.5 in 550 °C + 800 °C-WQ). The microstructures formed during heat treatments 550 °C + 950 °C-WQ (Fig. 6a) and 950 °C-WQ consist of primary laths with an average thickness of 1 μm and fine (0.2 μm average thickness) secondary laths in between. The microstructure of 550 °C + 950 °C-WQ and 950 °C-WQ is of acicular plate martensite morphology, Fig. 5a and b, which is typical of martensite in titanium alloys [7].

Additional tempering at 550 °C (950 °C-WQ + 550 °C) results in an increased size of the α lamellae colonies, increased thickness of individual α lamellae and growth of the β phase lamellae compared to the microstructure observed for the 950 °C-WQ specimen (Fig. 6a).

During cyclic heat treatment at 550 °C (950 °C-WQ + 4 cycles) a colony structure started to form (Fig. 6b). BSE (backscattered
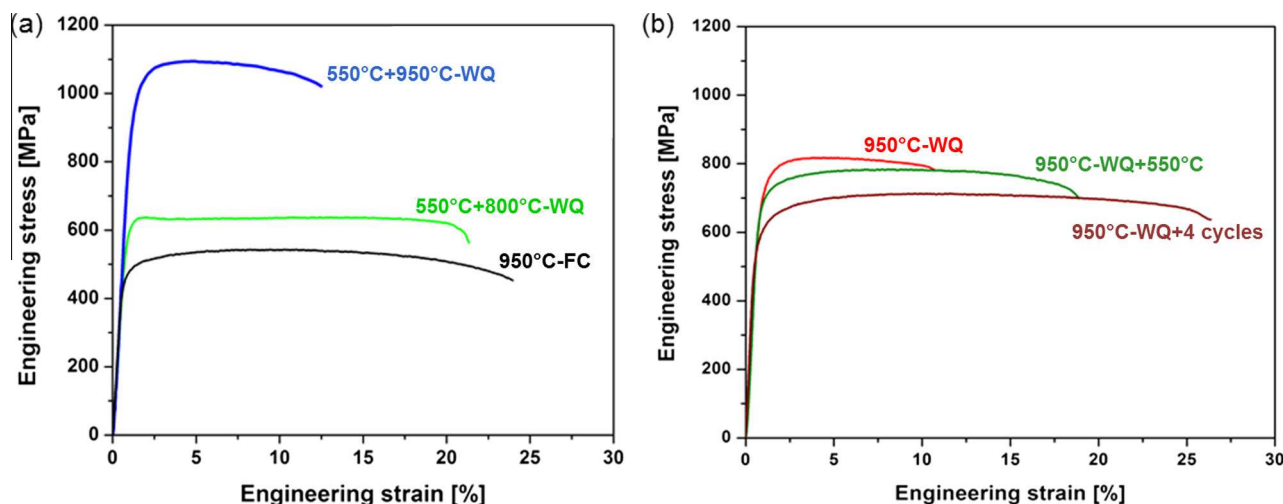

Fig. 3. Engineering stress–strain curves of Ti–4Mo subjected to (a) 950 °C-FC, 550 °C + 800 °C-WQ, 550 °C + 950 °C-WQ and (b) 950 °C-WQ, 950 °C-WQ + 550 °C, 950 °C-WQ + 4 cycles. An initial strain rate of $10^{-3}\ \mathrm{s}^{-1}$ was applied.
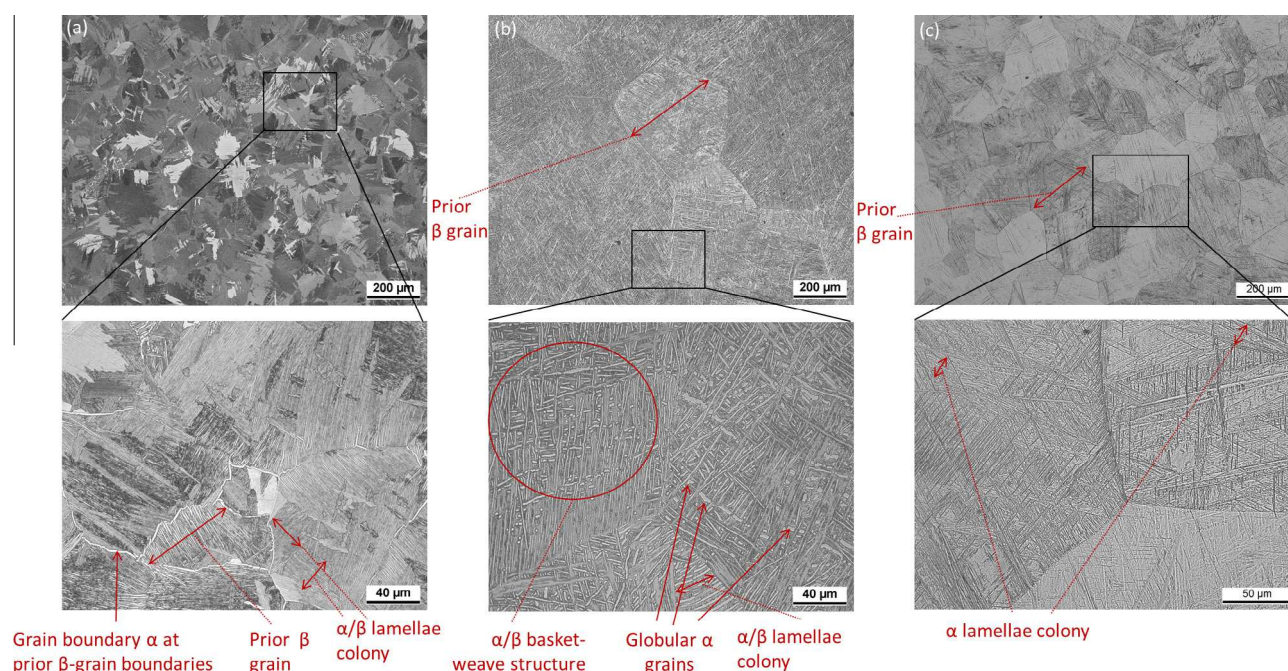
Fig. 4. Optical micrographs of the Ti–4Mo alloys after different types of heat treatments: (a) 950 °C-FC, (b) 550 °C + 800 °C-WQ, (c) 550 °C + 950 °C-WQ (see Fig. 2 and Table 2 for processing details). In 950 °C-FC (a) and 550 °C + 800 °C-WQ (b) the α phase exhibits bright contrast, in 550 °C + 950 °C-WQ (c) the fine α + β structure is not resolved, hence, appearing as an α colony structure.

electron) images and high resolution EBSD analysis of the cyclic heat treated material (950 °C-WQ + 4 cycles), Fig. 8, show fine (⩽200 nm) β layers in between the α laths (green arrows in Fig. 8). Some of the α laths started to break into α/β colonies (yellow arrows in Fig. 8).

TEM observations of Ti–4Mo subjected to heat treatment 950 °C-FC reveal a very fine lamellar structure with lamellae spacings down to the nanometer scale, Fig. 9a–c. Selected area diffraction (SAD) pattern taken from individual lamellae and the interfacial regions in between them show that the structure consists of alternating α and β lamellae with a near-Burgers OR between α and β (Fig. 9d)).

EBSD, TEM and X-ray diffraction (not shown here) data show that the martensite formed in Ti–4Mo water-quenched from 950 °C is of hexagonal type (α'). α' forms by nucleation and shear [36] inheriting the parent β-phase composition resulting in Mo super-saturation in the hexagonal martensite structure. The impingement of martensite plates produces localized distortion. In regions where the martensite transformation is substantially completed multiple impingement points where the martensite shear interacts with the interface lead to irregular interfaces of the primary plates as shown in the TEM micrographs in Fig 10.

Fig. 11 shows electron channeling contrast images (Fig. 11a and b) and bright-field transmission electron images (Fig. 11c) of Ti–4Mo after heat treatment 550 °C + 950 °C-WQ. The micrographs show the presence of substructures inside the martensite plates. Areas between the acicular laths show lamellae colonies of massive type martensite for both, primary and secondary plates.

TEM observations of the martensite substructures confirm the presence of α' accommodation twins and bcc β phase inside the α' plates. EBSD and TEM analysis of several martensite laths identify the α' accommodation twins as $\{10\bar{1}2\}$ tensile and $\{10\bar{1}1\}$ compression twins (Fig. 12).

TEM observations of the tempered Ti–4Mo sample (950 °C-WQ + 550 °C) (Fig. 13 and Fig. 14a) show the presence of secondary α precipitates within the primary α' plates. The diffraction pattern in Fig. 13 stem from one of the α lamellae shown in the bright field micrographs, revealing the presence of several undistorted α precipitates with a slight misorientation around $\{10\bar{1}0\}$.

Additionally, 20–40 nm thick β layers are observed at the α' plate boundaries. To analyze elemental segregation and partitioning APT tips were prepared by using site-specific FIB [31,32] extracting the APT specimens perpendicular to the laths of a colony. Mo-enriched layers with ∼20 nm size are found in the reconstructed APT data (Fig. 14b). These layers are identified as β phase by correlated TEM. Using 1-D composition profile analysis taken along a cylindrical region of interest (diameter: 10 nm, length: 90 nm) perpendicular to the interfaces the Mo enrichment in the β layers is found to be about 20 at% (Fig. 14c). The APT data show that none of the various heat treatments applied in this study lead to complete mesoscale chemical equilibrium states, however, near-equilibrium partitioning of Mo is indeed observed at the nanoscale where the two phases are abutting.

4. Discussion

4.1. Effects of annealing temperature and cooling rate on the microstructural evolution

Annealing at 950 °C followed by furnace cooling (950 °C-FC) results in the formation of a transformed β structure, consisting of colonies of α/β lamellae and grain boundary α phase, Figs. 4a, 5a, and 9. The colonies are clusters of α-laths pertaining to the same crystallographic variant, Fig. 5a. This indicates a diffusional mode of transformation. The alloying element molybdenum is a β-stabilizer and tends to partition to the β-phase during transformation [1–3,6–8,33,34]. The cooling rate from the homogenization temperature determines the width of the α-lamellae in the lamellar structure within the β grains and the extent of continuous α-layers at β grain boundaries [21]. Upon slow cooling below the β-transus temperature the α phase, which is incoherent with
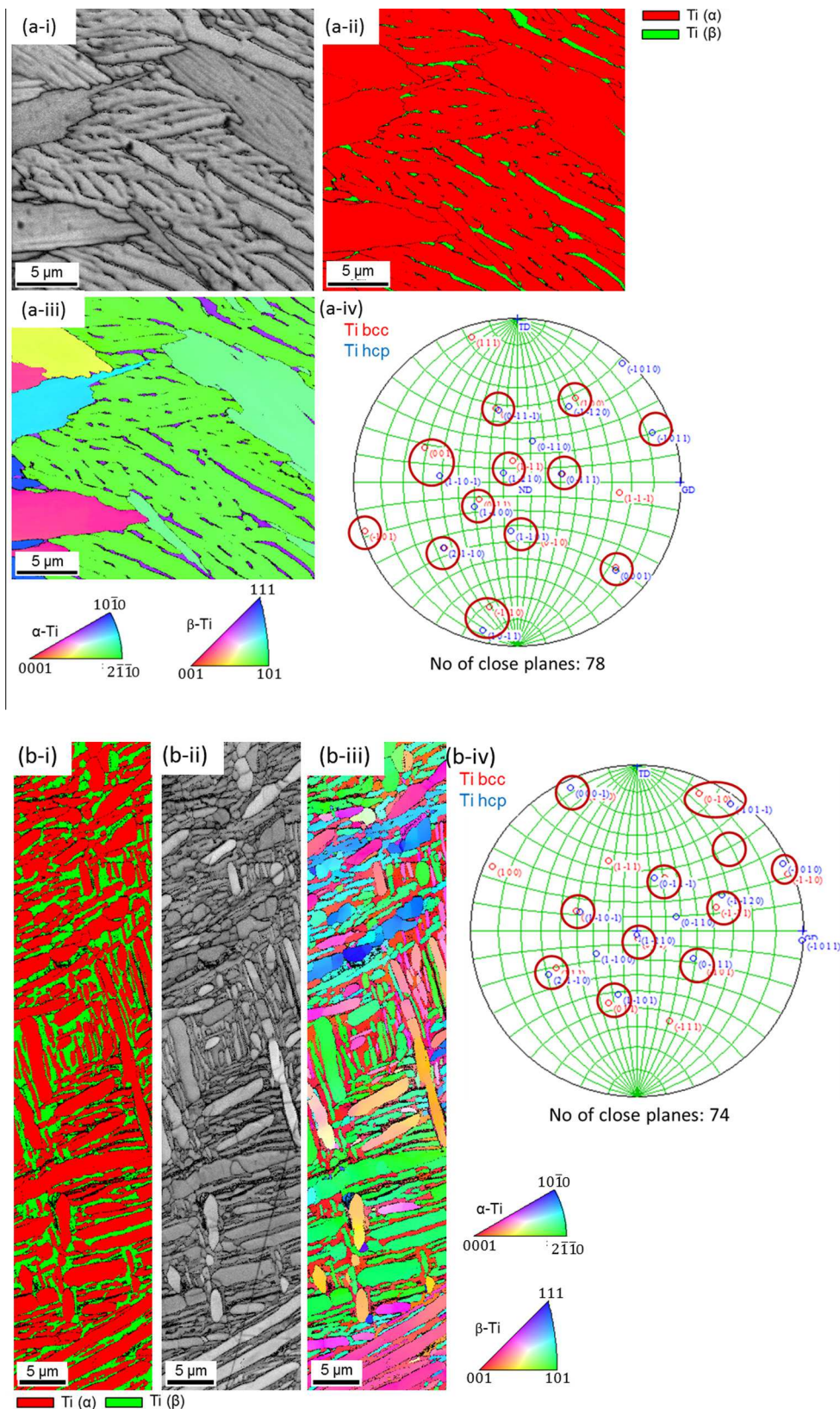
Fig. 5. (i) EBSD image quality (IQ), (ii) corresponding phase and (iii) inverse pole figure (IPF) maps of Ti–4Mo after the heat treatments: (a) 950 °C-FC, (b) 550 °C + 800 °C-WQ (see Fig. 2 and Table 2 for processing details), The stereographic projections (iv) are calculated from EBSD results (i–iii) showing the number of close planes between the two phases according to the Burger orientation relationship (BOR); the calculations were performed with a maximum plane misorientation of 2°.

respect to the β phase, is first nucleated along β-grain boundaries and thickened by growing into the respective β-grains. This leads to continuous α layers along the β grain boundaries, see Fig. 4a.

With further cooling α plates nucleate either at the interface of α layers or at the β grain boundary resulting in colonies of alternating lamellae of α and retained β matrix, Figs. 4a, 5a, and 9 [4,7].
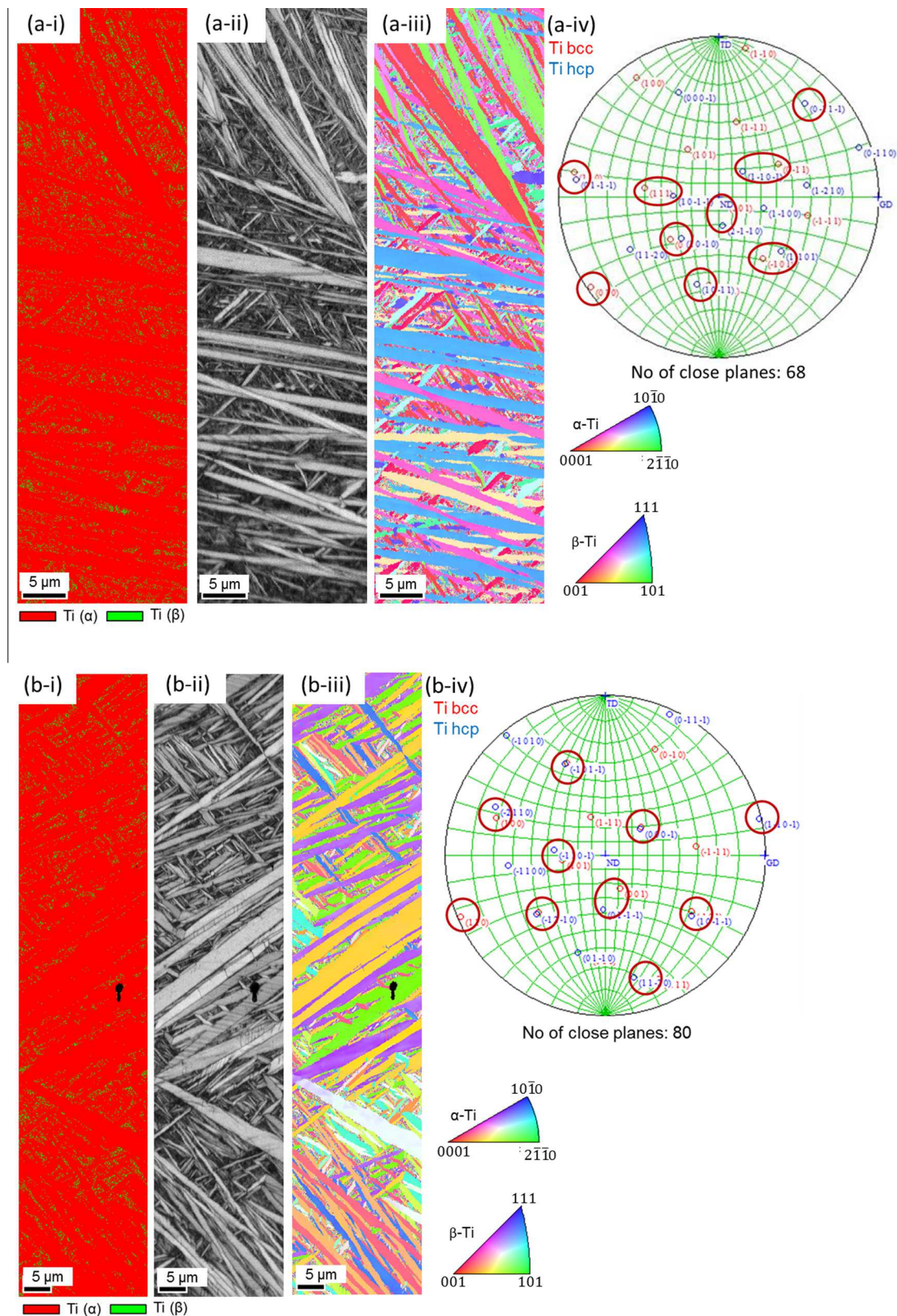
Fig. 6. (i) EBSD image quality (IQ), (ii) corresponding phase and (iii) inverse pole figure (IPF) maps of Ti–4Mo after the heat treatments: (a) 550 °C + 950 °C-WQ, (b) 950 °C-WQ (see Fig. 2 and Table 2 for processing details), The stereographic projections (iv) are calculated from EBSD results (i-iii) showing the number of close planes between the two phases according to the Burger orientation relationship (BOR); the calculations were performed with a maximum plane misorientation of 2°.

By increasing the cooling rate from the β-phase field (water quenching, heat treatments 550 °C + 950 °C-WQ and 950 °C-WQ) the Ti–4Mo transforms to α′ martensite with a hexagonal crystal structure, Fig. 6a and b. The observed martensite morphology is a mixture of massive and acicular martensite with β-layers at some of the martensite plate boundaries, Fig. 6a and b. It has been
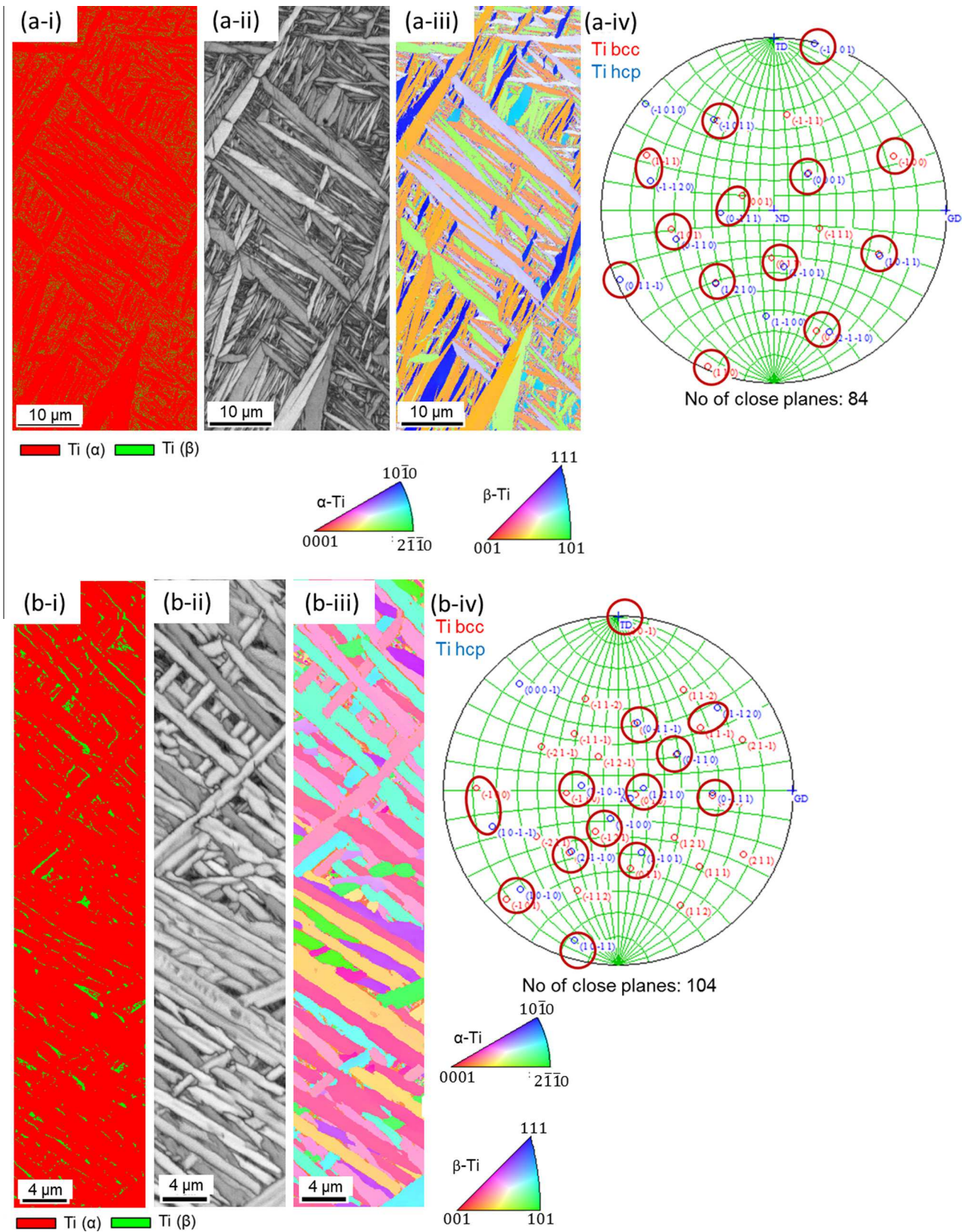
Fig. 7. (i) EBSD image quality (IQ), (ii) corresponding phase and (iii) inverse pole figure (IPF) maps of Ti–4Mo after the heat treatments: (a) 950 °C-WQ + 550 °C, (b) 950 °C-WQ + 4 cycles (see Fig. 2 and Table 2 for processing details), the stereographic projections (iv) are calculated from EBSD results (i–iii) showing the number of close planes between the two phases according to the Burger orientation relationship (BOR); the calculations were performed with a maximum plane misorientation of 2°.
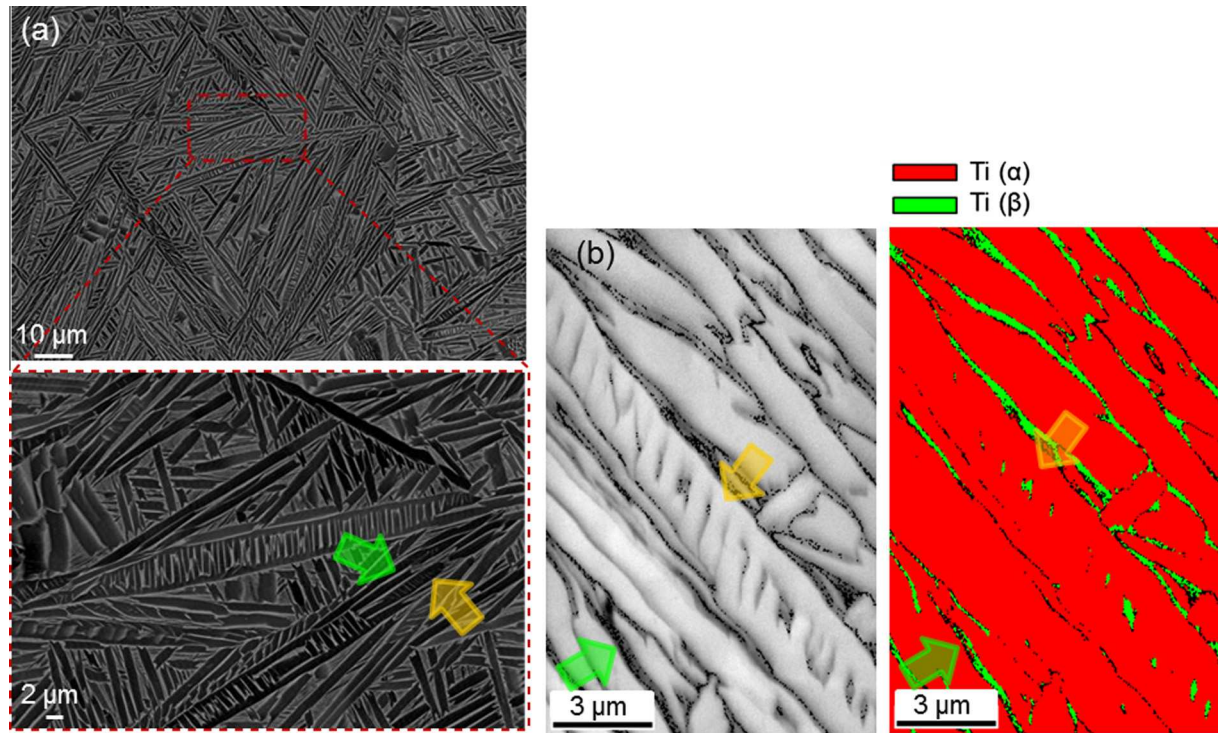
Fig. 8. (a) Backscattered electron (BSE) images of Ti–4Mo after cyclic treatment from the water quenched state (950 °C-WQ + 4 cycles), (b) corresponding EBSD IQ and phase map showing β phase inside the α laths. In the BSE micrographs (a) α phase exhibits a brighter contrast and β phase a darker contrast; in the IQ map (b) α phase has a darker contrast and β phase a brighter contrast.
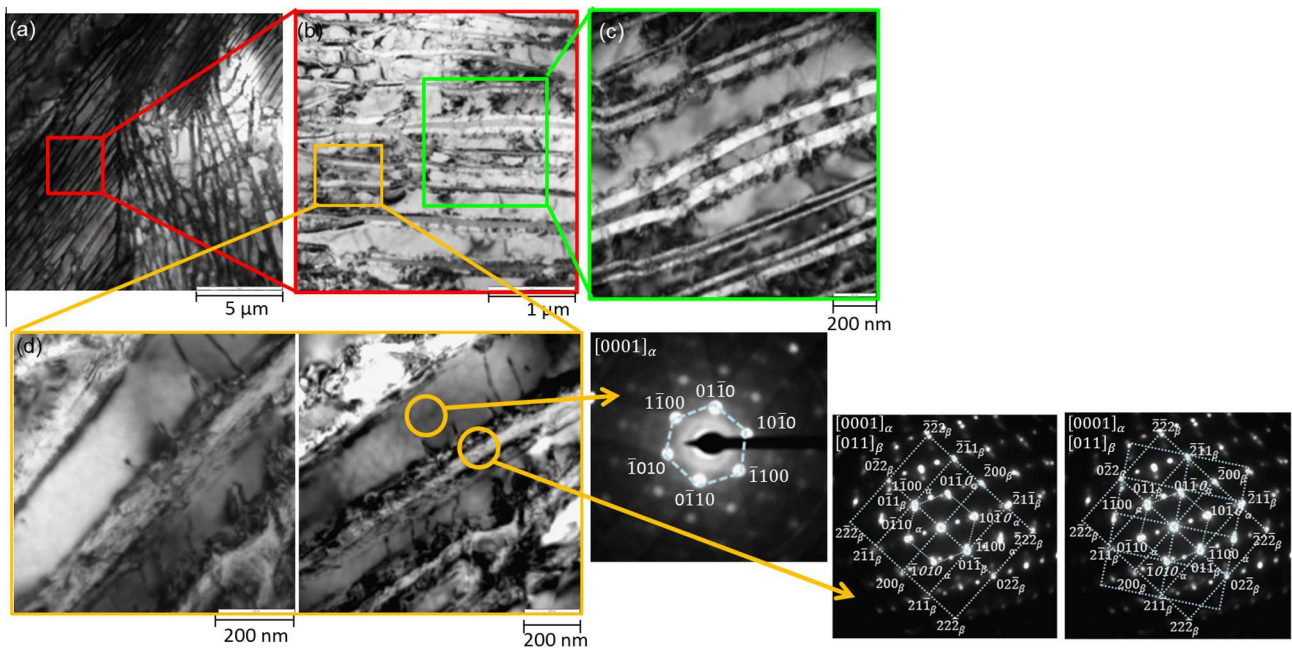

Fig. 9. Bright-field transmission electron micrographs of Ti–4Mo 950 °C-FC and convergent beam electron diffraction (CBED) patterns ([0 0 0 1]$_\alpha$ and [1 1 0]$_\beta$) showing alternating α and β lamellae with near-Burgers orientation relationship between the two phases.

reported [35] that molybdenum is very effective in producing acicular martensite and that the transition from massive to acicular martensite is completed for binary compositions above 4 wt% Mo. The evolution of the martensitic structure is discussed in further detail in Section 4.1.1.

During quenching from 800 °C (550 °C + 800 °C-WQ) the volume fraction of transformed α phase increases, however, a higher volume fraction of β phase is retained and the lamellar structure is coarser (Figs. 4b and 5b) which we ascribe to the kinetics of the β-to-α phase transformation. Generally, the annealing temperature and cooling rate determine the volume fraction of the recrystallized α phase [21]. It was reported before [35] for Ti-811 (Ti–8Al–1Mo–1V) that β transforms to martensite when quenched from 950 °C but is retained as bcc β when quenched
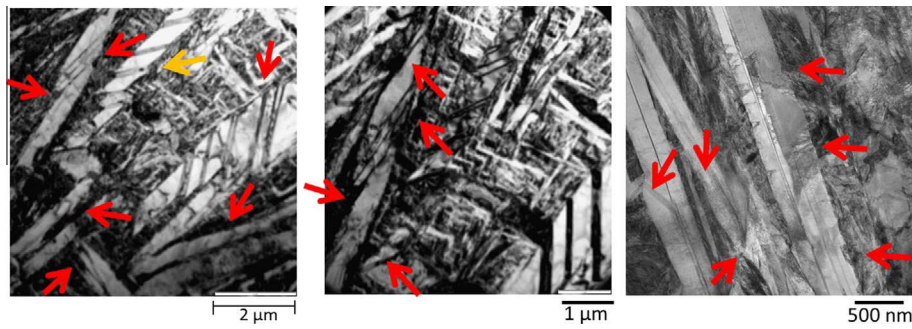
Fig. 10. TEM bright-field micrographs showing the structure and interfaces of primary and secondary martensite plates of 550 °C + 950 °C-WQ. Irregular interfaces of the primary martensite plates are marked by red arrows. The yellow arrow points at a primary plate boundary with a "step-like" interface structure. (For interpretation of the references to color in this figure legend, the reader is referred to the web version of this article.)
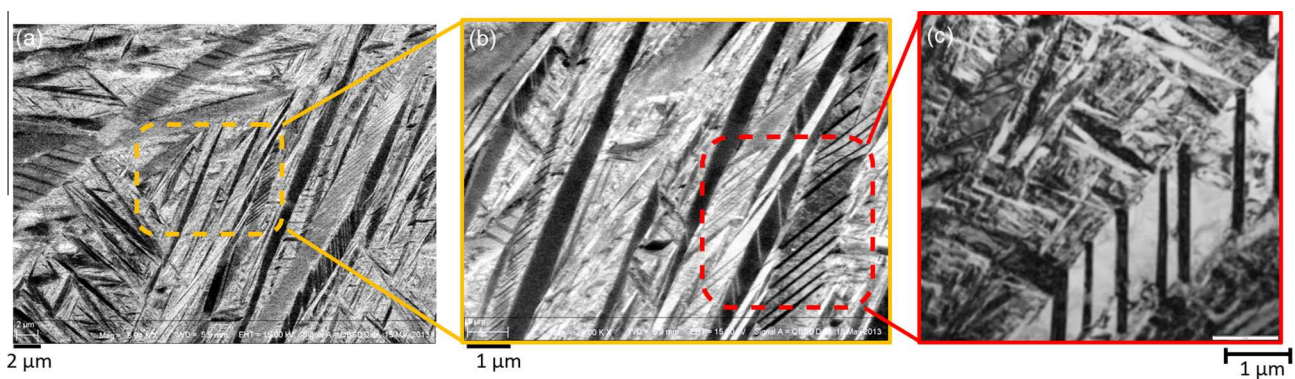

Fig. 11. (a, b) Electron channeling contrast images and c) bright-field transmission electron micrograph of Ti–4Mo after heat treatment 550 °C + 950 °C-WQ revealing the substructure inside martensite plates. The contrast is due to the crystallographic orientation.
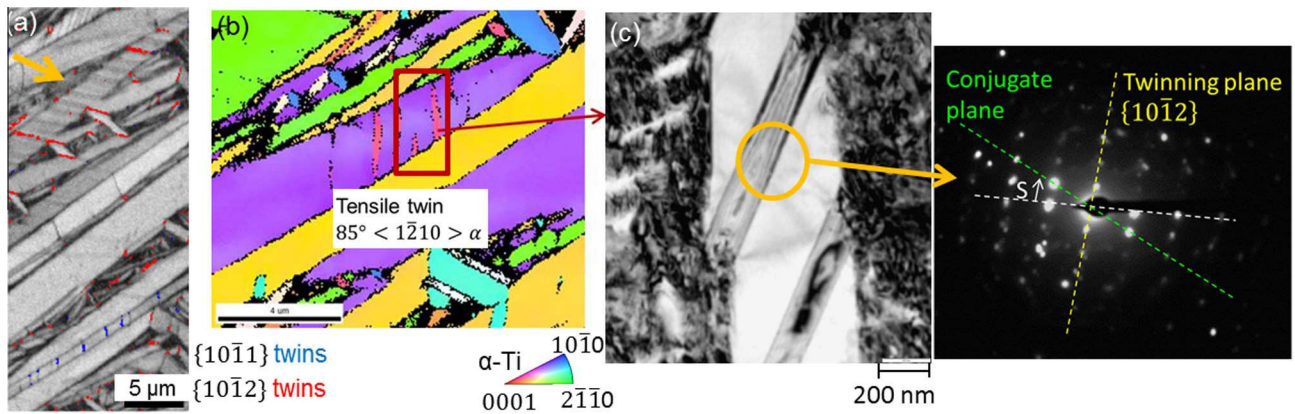

Fig. 12. (a) Image quality (IQ) and (b) inverse pole figure (IPF) map of sample 550 °C + 950 °C-WQ showing {10$\bar{1}$2} (tensile) and {10$\bar{1}$1} (compression) accommodation twins in Ti–4Mo (IPF map), (c) bright-field transmission electron micrographs and selected area diffraction pattern taken from a single plate showing {10$\bar{1}$2} (tensile) accommodation twins inside the martensite plate. The yellow arrow shows the "step-like" interface structure of an accommodation twinned martensite plate. (For interpretation of the references to color in this figure legend, the reader is referred to the web version of this article.)

from 800 °C. Annealing in the α + β field (800 °C, heat treatment 550 °C + 800 °C-WQ) produces a microstructure with primary α phase surrounded by retained β phase, Figs. 4b and 5b. The recrystallized β phase penetrates into recrystallized α lamellae along the α/α grain boundaries, Fig. 5b. During separation into α and β partitioning of the alloying element Mo, which is a strong β stabilizer, into the β phase was observed, Fig. 15. The solutes are quenched into the β phase during cooling and the β phase is thus preserved at room temperature.

4.1.1. Martensitic transformation and structures

Decomposition of the high temperature bcc β-phase upon cooling may proceed via diffusional, shear or mixed diffusional and shear modes [36]. Water-quenching from 950 °C produces a martensitic microstructure (550 °C + 950 °C-WQ and 950 °C-WQ), Figs. 4c and 6a,b. Our current microstructure observations show that some of the larger (1-2 μm thickness) martensite plates of Ti–4Mo 550 °C + 950 °C-WQ consist of a number of parallel plates separated by sub-boundaries representing a morphology between
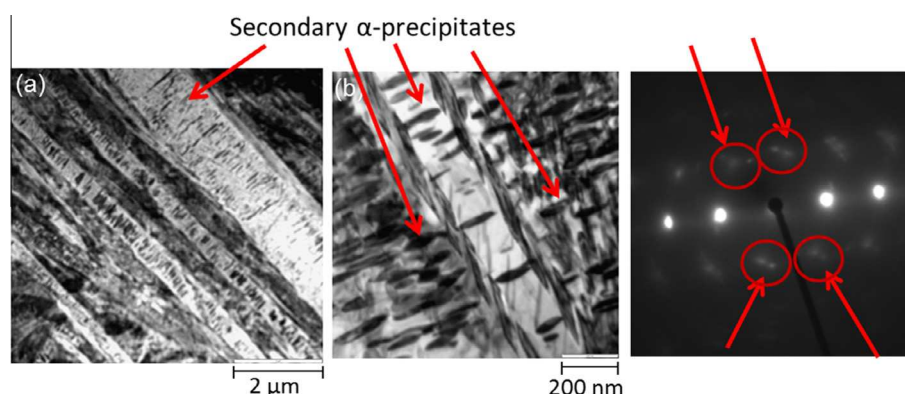
Fig. 13. (a) Bright-field transmission electron micrographs of Ti–4Mo 950 °C-WQ + 550 °C, (b) magnified region of (a) and corresponding diffraction pattern, revealing the presence of secondary α precipitates in α′ martensite.

massive colonies and single crystalline acicular martensite plates, Figs. 4c and 6a,b. The presence of colonies of secondary plates with massive morphology between primary acicular martensite plates is assumed to result from the local release of latent heat as the primary plates are formed. The martensite plates contain a high number of $\{10\bar{1}2\}$ and $\{10\bar{1}1\}$ accommodation twins, Fig. 12. We assume that the shear strain associated with $\{10\bar{1}2\}$ and $\{10\bar{1}1\}$ twinning (0.171 and 0.101, respectively [7]) causes the observed step-like appearance of accommodation twins with martensite plate boundaries [37–39], see e.g. the yellow arrows in Figs. 10 and 12.

Davis et al. [36] conducted a detailed study on a series of Ti–Mo alloys containing up to 10 wt% Mo, water-quenched from the β-phase region. They assumed that Mo segregated to the β-phase during quenching and concluded that, although shear holds the main contribution during the transformation, diffusion also plays a role in the nucleation and growth of martensitic structures in Ti4-Mo. Contrary to this study [36] we observed no Mo partitioning but a homogeneous Mo distribution in Ti4-Mo 550 °C + 950 °C-WQ and Ti4-Mo 950 °C-WQ using EDX and APT. In Fig. 16 we show EBSD-EDS and APT analysis of the 550 °C + 950 °C-WQ sample and high resolution TEM-EDX analysis of 950 °C-WQ. APT analysis and TEM-EDX analysis were performed at α/β interfaces. The APT tips were prepared via a site-specific FIB method [31,32], extracting the specimen parallel to the α/β interfaces. No Mo partitioning but a homogenous solid solution was observed for both conditions, 550 °C + 950 °C-WQ and 950 °C-WQ, indicating a displacive martensitic transformation upon quenching. It should be noticed here that the statistical relevance is low in the case of APT analysis; however, these results indicate a non-diffusional martensitic transformation upon quenching in the present study.

Martensitic structures in titanium alloys decompose when a quenched alloy is subjected to subsequent heat treatments [40]. The decomposition reaction occurs above the M_f temperature[1] and depends on the martensite crystal structure and the alloy composition [40]. Tempering of α′ martensite in β-isomorphous alloys was reported to proceed through α′ → α + β causing the precipitation of secondary α and β [40]. β was reported to nucleate heterogeneously at the α′ plate boundaries with a very coarse distribution [40]. Williams et al. [41] found no significant strengthening by these precipitates. Our observations show that such decomposition occurs already after 30 min tempering at 550 °C, Figs. 13 and 14. The TEM analysis shows the presence of secondary α and β phase precipitates and lamellae in the tempered structure, Figs. 13 and 14. The decomposition reaction involves Mo diffusion and partitioning as revealed by APT analysis, Fig. 14. Tempering and decomposition of the α′ martensite results in slightly decreased strength and significantly enhanced ductility, Fig. 3. This observation indicates that solid solution and martensite distortion affect the alloy's strength more than the formation of β precipitates in the present case.

During cyclic heat treatment at 550 °C (950 °C-WQ + 4 cycles) an α/β colony structure starts to form, Fig. 7b. β nucleates at the primary α′ lath boundaries and the existing boundary β grows in thickness, Fig. 7b. The β phase precipitates inside some of the primary α′ laths are assumed to have nucleated from twin boundaries inside the laths.

4.2. Relationship between the microstructures and the mechanical properties

Fig. 17 shows the tensile mechanical properties of the investigated Ti–4Mo alloys for the different applied heat treatments. For comparison the mechanical properties of grade 1 CP Ti and grade 2 CP Ti are also shown.

According to [7] grade 1 commercially pure (CP) titanium exhibits an ultimate tensile strength (UTS) of 240 MPa with 24% total elongation and grade 2 CP Ti an UTS of 345 MPa and 20% elongation, respectively (CP: commercial purity standard). Our study shows that by minor alloying and appropriate heat treatment significant modifications of the mechanical properties can be achieved.

The main source of strength, strain incompatibility, and stress inhomogeneity in titanium alloys are the α/β interfaces acting as barriers against dislocation motion [4,42,43]. Generally, the β-grain size, size of the colonies of α-phase lamellae, thickness of the α-lamellae and the interlamellar interface character are considered as important microstructural parameters determining the mechanical properties of α/β Ti alloys [21,22].

It was shown that the peak stress values for transformed microstructures at low strain follow a Hall–Petch dependence on the lath thickness [5,12]. Therefore, we assume that a similar Hall–Petch behavior was active in the two-phase α–β titanium alloys with Widmanstätten and/or colony α microstructures; meaning that the Hall–Petch effect was controlled by the properties and thickness of the α laths and platelets. The α colony size determines the effective slip length in lamellar microstructures across similarly oriented laths [12,44]. The width of the α lamellae and the colony size in Widmanstätten structures (550 °C + 950 °C-WQ, 950 °C-WQ) are significantly smaller than in α/β colony structures (950 °C-FC, 550 °C + 800 °C-WQ),

---

[1] M_f temperature: Martensite finish temperature, temperature at which the β-to-α′-martensite-transformation finishes during cooling.
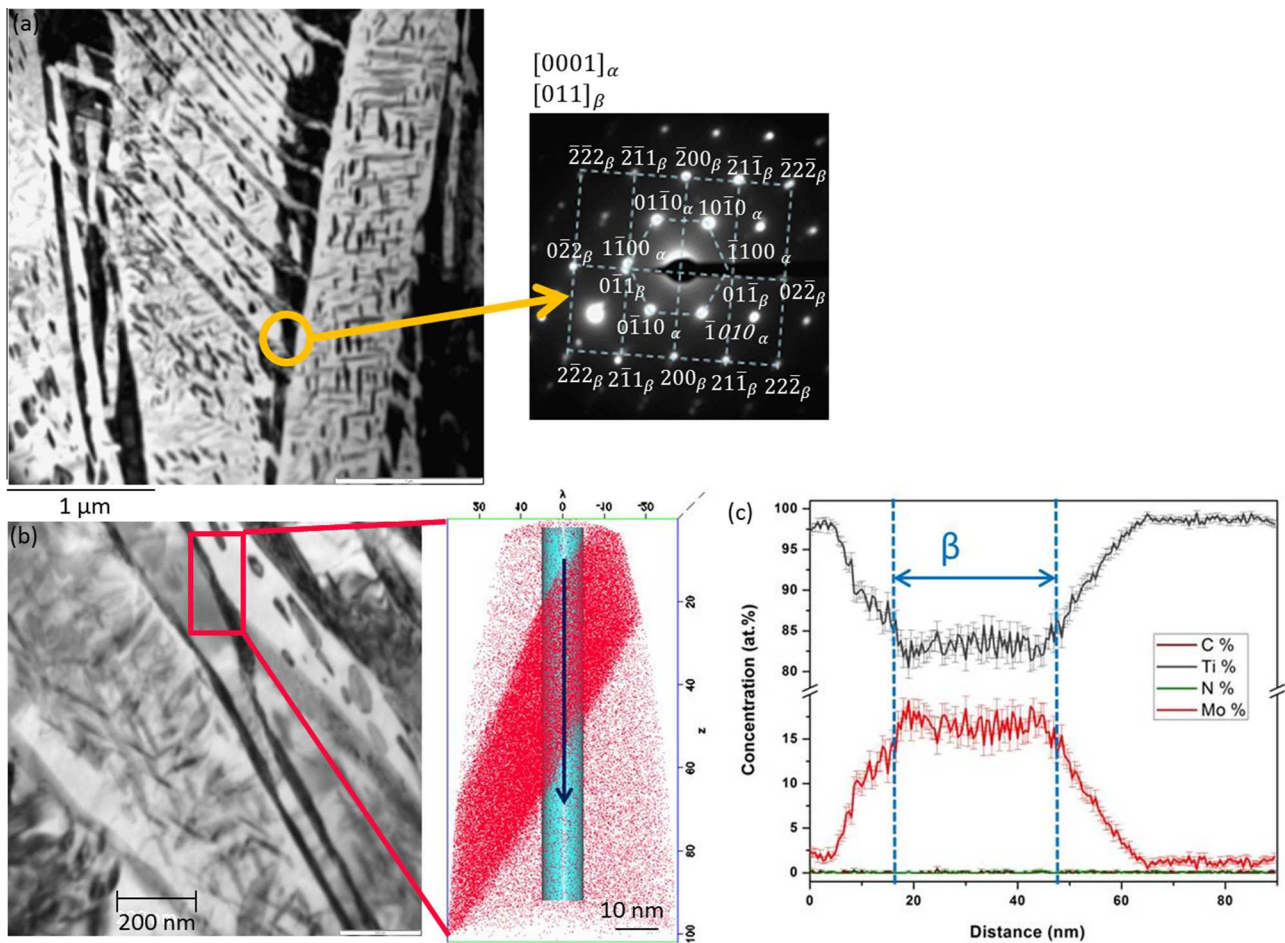
Fig. 14. (a) Bright-field transmission electron micrograph and selected area diffraction pattern depicting the near-Burgers orientation relationship observed between the α (hcp) and β (bcc) phases in Ti–4Mo after heat treatment 950 °C-WQ + 550 °C. (b) TEM bright field image, APT elemental map showing Mo atoms and (c) the corresponding 1-D concentration profile (bin width 0.5 nm) across the Mo enriched layer (cylindrical region of interest in (b)) showing very pronounced partitioning of Mo (red) of about 20 at% into a ~20 nm thick β lamellar zone, strongly enhancing its stability against phase transformation. (For interpretation of the references to color in this figure legend, the reader is referred to the web version of this article.)

Figs. 4–6, presumably causing the observed enhanced tensile strength. At the same time it was reported that microcracks often nucleate at grain boundaries and α/β phase boundaries due to the local stress field induced by dislocation accumulations and pile-ups [44,45], which is assumed to be the reason for the observed reduction in ductility.

Another reason for the ductility enhancement of Ti4Mo 950 °C-FC and Ti4Mo550 °C + 800 °C-WQ with respect to Ti4Mo 550 °C + 950 °C-WQ is the volume fraction of the β-phase [46]. In Ti alloys α and β phases are both ductile and it is generally assumed that the α-phase is softer than the β-phase and, hence, dislocation slip is initiated in the α-phase [4,35,45]. Even though slip initiates in the softer of the two lamellar phases and impinges on the harder phase, macroscopic yielding occurs when a slip system, once activated in the softer phase, has the ability to shear the harder phase [35]. However, with increasing volume fraction of the β phase the effective length scale reduces and eventually eliminates the plastic constraint. Then it is likely that this phase will become the softer of the two phases initiating dislocation slip [4].

By comparing the properties of Ti–4Mo quenched from the β region (950 °C) with and without prior holding at 550 °C (550 °C + 950 °C-WQ and 950 °C-WQ) we observe that annealing at 550 °C before β annealing increases the tensile strength without any significant decrease in ductility. Holding at 550 °C for 6 h leads
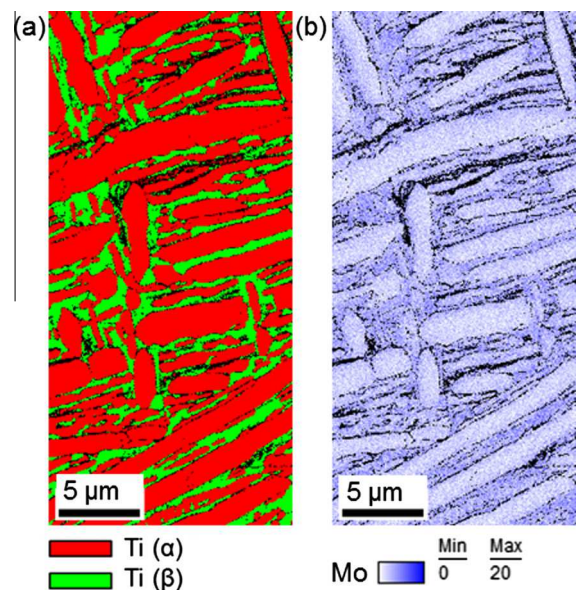

Fig. 15. (a) EBSD phase map and (b) corresponding EDS map for Mo of Ti–4Mo after heat treatment 550 °C + 800 °C-WQ. The data clearly reveal the partitioning of Mo into the bcc β phase promoting its stability.
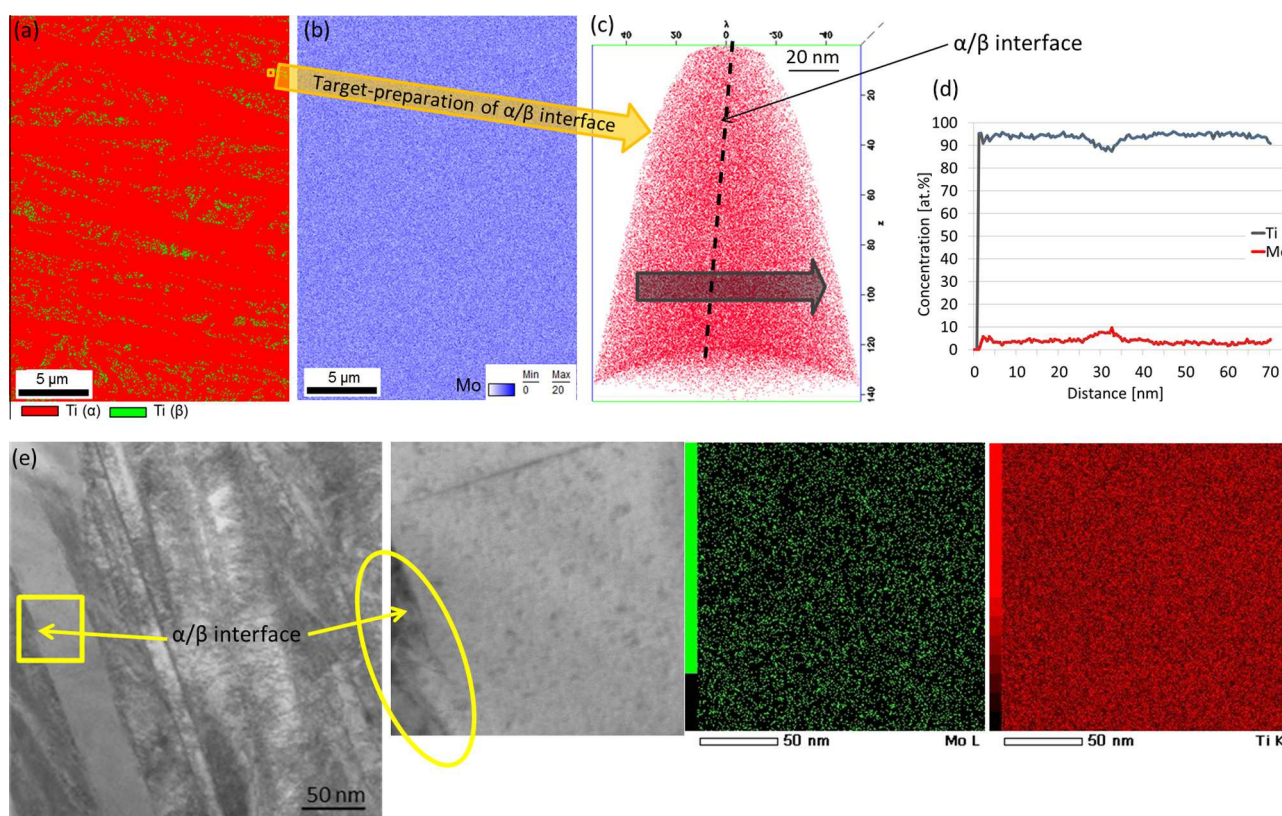
Fig. 16. SEM-EDX and corresponding phase map (a) of 550 °C + 950 °C-WQ, Mo EDX map (b), (c) APT elemental map showing Mo atoms and (d) the corresponding 1-D concentration profile (bin width 0.5 nm) of 550 °C + 950 °C-WQ. The APT tip was prepared site specific with an α/β interface vertically aligned in the tip. (d) High resolution TEM-EDX analysis of an α/β interface in 950 °C-WQ. No Mo partitioning but solid solution is revealed for 550 °C + 950 °C-WQ and 950 °C-WQ.
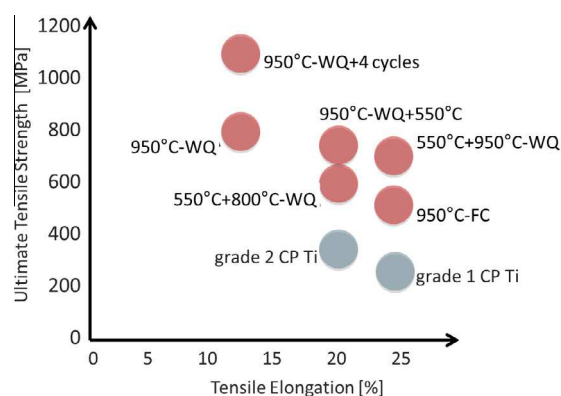

Fig. 17. Tensile mechanical properties of Ti–4Mo after different heat treatments conducted in this work compared with grade 1 and 2 CP titanium [7]; (CP: commercial purity standard).

to a high Mo concentration and homogeneous Mo distribution in the α phase causing a finer microstructure after quenching from the β region and, hence, higher strength. Generally, massive accommodation twinning is observed in the martensitic structures of Ti–4Mo 550 °C + 950 °C-WQ and Ti–4Mo 950 °C-WQ, Figs. 11 and 12, leading to structural refinement. Besides the martensitic distortion this structural refinement is supposed to contribute to the lower uniform elongation and higher strength. Tempering of the martensitic structure (950 °C-WQ + 550 °C) leads to an increase in the lath thickness (Fig. 7a), growth of the β phase (Fig. 7a), and relaxation of the distorted martensitic structure. These factors result in a reduction of the tensile strength and increase in tensile

elongation when compared to the primary martensitic structures (550 °C + 950 °C-WQ and 950 °C-WQ).

When applying a cyclic heat treatment β layers systematically form in between the α laths and the primary α laths start to break into smaller colonies subdivided by β films, Figs. 7b and 8. We assume that the twin boundaries inside the laths are acting as preferential nucleation sites for β. When comparing the quenched state (950 °C-WQ) with cyclic heat treated samples (950 °C-WQ + 4 cycles) a slight decrease in strength (from 800 MPa to 700 MPa) with a doubling in tensile elongation (from 12% to about 25%) was achieved. Such finely scaled laminate metallic dual phase microstructures consisting of a martensite matrix and reverted austenite layers were also earlier reported to increase both, ductility and strength at the same time in a Fe–Mn steel [47].

5. Conclusions

(1) A broad variety of different mechanisms and kinetics of microstructure formation including diffusion driven allotropic phase transformations as well as shear and/or diffusion dominated modes of martensitic transformations was observed in a simple binary Ti–4Mo alloy. Depending on the applied heat treatment the topology, size and chemistry of α, β, α' phases can be varied leading to a wide spectrum of mechanical properties.

(2) Variation in the heat treatment parameters (annealing temperature and cooling rate) enable accessing the full range of mechanical properties from low strength and high ductility (500 MPa, 25% elongation) to high strength and lower ductility (1100 MPa, 12% elongation) in a binary near-α Ti–Mo alloy. Laminate dual phase

microstructures obtained by tempering and thermal cycling increase both, strength and ductility at the same time.

(3) Water quenching from the β phase region (950 °C) causes the formation of hexagonal type (α′) martensite, showing a tensile strength of 1100 MPa at 12% elongation. This is attributed to the reduction of α colony size and martensite formation.

(4) β transforms to α′ martensite when the alloy is quenched from the β-phase field (950 °C) but it is retained as bcc β when quenched from the two phase region (800 °C).

(5) The martensitic structures in Ti–4Mo represent a morphology intermediate between massive colonies and acicular martensite plates. It is found that shear and diffusional components contribute to the transformation of Ti–4Mo depending on the cooling rate.

(6) Tempering and cyclic heat treatment of quenched Ti–4Mo cause microstructure coarsening and tempering of the martensite resulting in a minor decrease in strength but significant increase in ductility.

(7) We observed that none of the various heat treatments applied in this study lead to complete mesoscale chemical equilibrium states, however, near-equilibrium partitioning of Mo is indeed observed at the nanoscale where the two phases are abutting.

References

[1] E.W. Collings, The Physical Metallurgy of Titanium Alloys, American Society of Metals, 1984.
[2] R. Boyer et al., Materials Property Handbook: Titanium Alloys, ASM International, 1994.
[3] S.L. Semiatin, V. Seetharaman, I. Weiss, Advances in Science and Technology of Ti Alloy Processing, Metals and Materials Society, The Minerals, 1997.
[4] D. Banerjee, J.C. Williams, Acta Mater. 61 (2013) 844–879.
[5] S.L. Semiatin, T.R. Bieler, Acta Mater. 49 (2001) 3565–3573.
[6] G. Lütjering, J. Albrecht, O.M. Ivasishin, in: Proceedings of the Titanium'95: Science and Technology, TMS, 1995, pp. 1163–1170.
[7] G. Lütjering, J.C. Williams, Titanium, 2nd ed., Springer, Berlin, 2007.
[8] C. Leyens, M. Peters, Titanium and Titanium Alloys, Wiley-VCH, Weinheim, 2003.
[9] B. Liu, Y.P. Li, H. Matsumoto, Y.B. Liu, Y. Lib, A. Chiba, Mater. Sci. Eng., A 528 (2011) 2345–2352.
[10] S. Banerjee, P. Mukhopadhyay, Phase Transformations, Examples from Titanium and Zirconium Alloys, Elsevier, Oxford, 2007.
[11] T. Ahmed, H.J. Rack, Mater. Sci. Eng., A 243 (1998) 206–211.
[12] J. Tiley, T. Searles, E. Lee, S. Kar, R. Banerjee, J.C. Russ, H.L. Fraser, Mater. Sci. Eng., A 372 (2004) 191–198.
[13] D. He, J. Zhu, S. Zaefferer, D. Raabe, Mater. Des. 56 (2014) 937–942.
[14] L. He, A. Dehghan-Manshadi, R.J. Dippenaar, Mater. Sci. Eng., A 549 (2012) 163–167.
[15] S.L. Semiatin, V. Seetharaman, I. Weiss, Mater. Sci. Eng., A 263 (1999) 257–271.
[16] L. Wang, R.I. Barabash, Y. Yang, T.R. Bieler, M.A. Crimp, P. Eisenlohr, W. Liu, G.E. Ice, Metall. Mater. Trans. A 42 (2011) 626–635.
[17] T.R. Bieler, S.L. Semiatin, Int. J. Plasticity 18 (2002) 1165–1189.
[18] C.C. Tasan, M. Diehl, D. Yan, C. Zambaldi, P. Shanthraj, F. Roters, D. Raabe, Acta Mater. 81 (2014) 386–400.
[19] C.C. Tasan, J.P.M. Hoefnagels, M. Diehl, D. Yan, F. Roters, D. Raabe, Int. J. Plasticity 63 (2014) 198–210.
[20] L. Zeng, T.R. Bieler, Mater. Sci. Eng., A 392 (2005) 403–414.
[21] G. Lütjering, Mater. Sci. Eng., A 243 (1998) 32–45.
[22] R. Filip, K. Kubiak, W. Ziaja, J. Sieniawski, J. Mater. Process. Technol. 133 (2003) 84–89.
[23] J.H. Kim, S.L. Semiatin, C.S. Lee, Acta Mater. 51 (2003) 5613–5626.
[24] S.V. Zherebtsov, G.A. Salishchev, R.M. Galeyev, O.R. Valiakhmetov, S. Yu Mironov, S.L. Semiatin, Scripta Mater. 51 (2004) 1147–1151.
[25] D. He, J.C. Zhu, S. Zaefferer, D. Raabe, Y. Liu, Z.L. Lai, X.W. Yang, Mater. Sci. Eng., A 549 (2012) 20–29.
[26] B. Sander, D. Raabe, Mater. Sci. Eng., A 479 (2008) 236–247.
[27] D.A. Porter, K.E. Easterling, Phase Transformations in Metals and Alloys, 2nd ed., Chapman and Hall, London, 1992.
[28] E. Pereloma, D.V. Edmonds (Eds.), Phase Transformations in Steels, Woodhead Publishing, Cambridge, 2012.
[29] D. Raabe, M. Sachtleber, Z. Zhao, F. Roters, S. Zaefferer, Acta Mater. 49 (2001) 3433–3441.
[30] K. Thompson, D. Lawrence, D.J. Larson, J.D. Olson, T.F. Kelly, B. Gorman, Ultramicroscopy 107 (2007) 131–139.
[31] M. Herbig, D. Raabe, Y.J. Li, P. Choi, S. Zaefferer, S. Goto, Phys. Rev. Lett. 112 (2014) 1–5.
[32] Y. Toji, H. Matsuda, M. Herbig, P.-P. Choi, D. Raabe, Acta Mater. 65 (2014) 215–228.
[33] D. Raabe, B. Sander, M. Friak, D. Ma, J. Neugebauer, Acta Mater. 55 (2007) 4475–4487.
[34] M. Friak, B. Sander, D. Raabe, J. Neugebauer, J. Phys.: Condens. Matter. 20 (2008).
[35] K.S. Chan, C.C. Wojcik, D.A. Koss, Metall. Trans. A 12 (1981) 1899–1907.
[36] R. Davis, H.M. Flower, D.R.F. West, J. Mater. Sci. 14 (1979) 712–722.
[37] D. Bhattacharyya, G.B. Viswanathan, R. Denkenberger, D. Furrer, H.L. Fraser, Acta Mater. 51 (2003) 4679–4691.
[38] J.C. Williams, R. Taggart, D.H. Polonis, Metall. Trans. 1 (1970) 2265–2270.
[39] R.H. Ericksen, R. Taggart, D.H. Polonis, Acta Metall. 17 (1969) 553–564.
[40] F.X. Gil Mur, D. Rodriguez, J.A. Planell, J. Alloys Compd. 234 (1996) 287–289.
[41] J.C. Williams, B.S. Hickman, Metall. Trans. 1 (1970) 2648–2650.
[42] S. Suri, G.B. Viswanathan, T. Neeraj, D.-H. Hou, M.J. Mills, Acta Mater. 47 (1999) 1019–1034.
[43] M.F. Savage, J. Tatalovich, M. Zupan, K.J. Hemker, M.J. Mills, Mater. Sci. Eng., A 319–321 (2001) 398–403.
[44] R. Liu, S. Hui, W. Ye, Y. Yu, Y. Fu, X. Song, X. Deng, Rare Met. 31 (2012) 420–423.
[45] T.R. Bieler, A. Fallahi, B.C. Ng, D. Kumar, M.A. Crimp, B.A. Simkin, A. Zamiri, F. Pourboghrat, D.E. Mason, Intermetallics 13 (2005) 979–984.
[46] Y. Liu, L.F. Chen, H.P. Tang, C.T. Liu, B. Liu, B.Y. Huang, Mater. Sci. Eng., A 418 (2006) 25–35.
[47] M.-M. Wang, C.C. Tasan, D. Ponge, A. Kostka, D. Raabe, Acta Mater. 79 (2014) 268–281.